

# Global Water Vapor Trend from 1988 to 2011 and Its Diurnal Asymmetry Based on GPS, Radiosonde, and Microwave Satellite Measurements

JUNHONG WANG

*Department of Atmospheric and Environmental Sciences, University at Albany, State University of New York, Albany, New York*

AIGUO DAI

*Department of Atmospheric and Environmental Sciences, University at Albany, State University of New York, Albany, New York, and National Center for Atmospheric Research, Boulder, Colorado*

CARL MEARS

*Remote Sensing Systems, Santa Rosa, California*

(Manuscript received 16 July 2015, in final form 7 April 2016)

## ABSTRACT

This study analyzes trends in precipitable water (PW) over land and ocean from 1988 to 2011, the PW–surface temperature  $T_s$  relationship, and their diurnal asymmetry using homogenized radiosonde data, microwave satellite observations, and ground-based global positioning system (GPS) measurements. It is found that positive PW trends predominate over the globe, with larger magnitudes over ocean than over land. The PW trend is correlated with surface warming spatially over ocean with a pattern correlation coefficient of 0.51. The PW percentage increase rate normalized by  $T_s$  expressed as  $d \ln PW / dT_s$  is larger and closer to the rate implied by the Clausius–Clapeyron (C–C) equation over ocean than over land. The 2-hourly GPS PW data show that the PW trend from 1995 to 2011 is larger at night than during daytime. Nighttime PW monthly anomalies correlate positively and significantly with nighttime minimum temperature  $T_{\min}$  at all stations, but this is not true for daytime PW and maximum temperature  $T_{\max}$ . The ratio of relative PW changes with  $T_{\min}$  ( $d \ln PW / dT_{\min}$ ) is larger and closer to the C–C equation's implied value of  $\sim 7\% \text{ K}^{-1}$  than  $d \ln PW / dT_{\max}$ . This suggests that the relationship between PW and  $T_s$  at night is a better indicator of the water vapor feedback than that during daytime, when clouds and other factors also influence  $T_s$ .

## 1. Introduction

Water vapor has the largest greenhouse effect on Earth's climate. However, the amount of water vapor in the atmosphere is controlled by air temperature, unlike other greenhouse gases, which are controlled by emissions (Myhre et al. 2013). Other greenhouse gases, primarily  $\text{CO}_2$ , impact the amount of water vapor in the atmosphere through modulating the air temperature. The strong coupling between water vapor content and air temperature provides the basis for a strong positive

water vapor feedback that amplifies the initial temperature changes induced by other greenhouse gases. Water vapor also plays a key role in the atmospheric hydrological cycle (Trenberth et al. 2003) by allowing winds to move water around Earth and by providing the water source for the formation of clouds and precipitation. It is also a key component in the global energy cycle through surface evaporation and atmospheric latent heating (Trenberth et al. 2009). Thus, it is important to understand water vapor variability and change and its relationship with temperature.

Despite the important role of water vapor in Earth's climate, reliable data of atmospheric water vapor are still lacking. Over the tropical oceans where long-term

---

*Corresponding author address:* Junhong (June) Wang, Department of Atmospheric and Environmental Sciences, University at Albany, SUNY, 1400 Washington Ave., Albany, NY 12222.  
E-mail: jwang20@albany.edu

---

*Publisher's Note:* This article was revised on 13 July 2016 to correct an editing error related to the citation of Fig. 13 in section 5.

microwave satellite measurements are available, atmospheric reanalysis products show precipitable water (PW) trends that are different from the satellite data from 1988 to 2012, and most climate models show much larger PW trends than the satellite observations (Flato et al. 2013), likely owing in part to different realizations of internal climate variability in models and observations. When the relative humidity (RH) in the lower troposphere stays constant, PW increases with air temperature by about  $7\% \text{ K}^{-1}$  (referred to as the scaling ratio) based on the Clausius–Clapeyron (C–C) relation (Trenberth et al. 2005). On the decadal time scale, the scaling ratio over the tropical oceans is tightly constrained in all model simulations but not in all observations and reanalyses (Mears et al. 2007; Flato et al. 2013). For the models, decadal-scale changes are due to a combination of forced changes and natural variability, leading to a wide range of trends in both PW and air temperature. Despite this, the models produce similar ratios, suggesting that on large spatial scales, the models are constrained by basic physics, as expected. The scaling-ratio discrepancies found in some observations and reanalyses are likely due to unresolved inhomogeneity in the observational data and/or reanalysis products. It is more challenging over land where the radiosonde humidity data are the main source of observations. Large errors in radiosonde humidity data may have contaminated many of the reanalysis and observational products (Dai et al. 2011). Dai et al. (2011, 2013) showed that the ERA-40 and NCEP–NCAR reanalysis products, which used the unhomogenized radiosonde temperature and humidity data, contain the same spurious changes in atmospheric temperature and water vapor seen in radiosonde station records. Thus, most current gridded water vapor products are not suitable for long-term change analyses, as the large inhomogeneities in radiosonde data were not removed in these analyses.

For the previous five Intergovernmental Panel for Climate Change (IPCC) assessment reports (ARs), only the last three show PW trend maps. The IPCC third AR (TAR) shows the trends at 214 radiosonde stations in the Northern Hemisphere, while the fourth AR (AR4) and fifth AR (AR5) only show the PW trends over ocean using the microwave satellite data. Overland radiosonde and ground-based GPS measurements are the primary data sources for PW. The inhomogeneity in the radiosonde record hampers its usage for long-term humidity trend estimates (e.g., Dai et al. 2011; Wang et al. 2013). The GPS PW data are available on a global scale only since the early 1990s and need to be processed consistently through the period (e.g., Wang et al. 2007). As a result, the PW trend over land and its

relationship with temperature changes have not been studied extensively.

There have been many studies on the diurnal asymmetry in surface temperature trends, which show stronger warming during nighttime than daytime (e.g., Karl et al. 1993; Easterling et al. 1997; Dai et al. 1999; Wang and Gaffen 2001; Vose et al. 2005; Isaac and Van Wijngaarden 2012). However, there have been only a few studies on differential trends in subdaily surface humidity, and they found stronger humidity trends at night than during the day (Gaffen and Ross 1999; Dai 2006; Shiu et al. 2009). There have been no studies on the diurnal asymmetry in precipitable water, partially owing to a lack of high-resolution data.

In this study, we focus on answering the following questions.

- 1) What is the best estimate of the global PW trend for recent years from 1988 to 2011 and its spatial variability over both land and ocean based on observations? To answer this question, we make use of three unique PW datasets—namely, the homogenized global radiosonde humidity dataset (Dai et al. 2011), the 2-hourly GPS PW dataset (Wang et al. 2007), and the newest version of the microwave satellite PW data over oceans (Wentz 1997; Wentz et al. 2007).
- 2) Can PW interannual variability and trends be explained by temperature changes on both global and regional scales, and if so, how? Most of the previous studies have used global-averaged time series to derive the scaling ratio, which normally follows the C–C relation (e.g., Wentz and Schabel 2000; Trenberth et al. 2005; Mears et al. 2007). Wagner et al. (2006) found that in the extratropics, the PW from one satellite product and surface temperature  $T_s$  for cloud-free conditions show almost no correlation both in spatial patterns of trends for 1996–2003 and in extratropical averaged monthly anomalies. O’Gorman and Muller (2010) show that the scaling ratio has significant spatial variability in climate change simulations.
- 3) What is the diurnal asymmetry of the PW trend and its relationship with  $T_s$ ? One of the advantages of the GPS PW data is their high temporal resolution, which enables us to study the PW diurnal asymmetry for the first time.

The datasets used in this study are described in section 2. Section 3 presents intercomparisons of PW trends and global PW trend analysis among the different datasets. This is followed by an analysis of correlation between PW and  $T_s$  variability in section 4. Section 5 focuses on the diurnal asymmetry of the PW trend and its relationship with  $T_s$ . A summary and conclusions are given in section 6.

TABLE 1. Characteristics of the datasets used in this study.

Name	Spatial coverage	Temporal resolution	Temporal coverage	Sources
2-hourly GPS PW	Global land stations	2-hourly	1995–2015	<a href="http://rda.ucar.edu/datasets/ds721.1/">http://rda.ucar.edu/datasets/ds721.1/</a>
PW (up to 100 hPa) from homogenized radiosonde data	Global land stations	Twice daily	1973–2012	Data available upon request from June Wang
MWR monthly mean PW data	Ocean $1^\circ \times 1^\circ$	Monthly	1988–present	<a href="ftp://ftp.remss.com/vapor/monthly_1deg/">ftp://ftp.remss.com/vapor/monthly_1deg/</a>
GHCN-M temperature dataset	Global land stations	Monthly	1701–present	<a href="http://www.ncdc.noaa.gov/ghcnm/v3.php">http://www.ncdc.noaa.gov/ghcnm/v3.php</a>
NOAA gridded monthly average temperature anomaly dataset	Global $5^\circ \times 5^\circ$	Monthly	1880–present	<a href="ftp://ftp.ncdc.noaa.gov/pub/data/ghcn/v3/grid/">ftp://ftp.ncdc.noaa.gov/pub/data/ghcn/v3/grid/</a>
ICOADS	Ocean $1^\circ \times 1^\circ$	Monthly	1960–present	<a href="http://icoads.noaa.gov/">http://icoads.noaa.gov/</a>
HadISDH	Land $5^\circ \times 5^\circ$	Monthly	1973–2015	<a href="http://www.metoffice.gov.uk/hadobs/hadisdh/">http://www.metoffice.gov.uk/hadobs/hadisdh/</a>
HadISD	Global land stations	Hourly	1973–2015	<a href="http://www.metoffice.gov.uk/hadobs/hadis/">http://www.metoffice.gov.uk/hadobs/hadis/</a>

## 2. PW datasets and analysis method

Three PW datasets are available from 1995 to 2011 and are used in this study. They include the 2-hourly GPS PW dataset (Wang et al. 2007), homogenized radiosonde (raob) dataset (Dai et al. 2011; Wang et al. 2013), and microwave (MWR) satellite data (Wentz 1997; Wentz et al. 2007). Their characteristics are summarized in Table 1. The 2-hourly GPS and twice-daily radiosonde data are available at stations over land, and monthly mean MWR satellite PW data are gridded onto a  $1^\circ \times 1^\circ$  grid over oceans. The GPS PW is derived from the tropospheric delay of radio signals from the GPS satellites to the ground GPS receivers and has a root-mean-square (RMS) error of less than 3 mm (Wang et al. 2007). The 2-hourly GPS PW data have been improved after Wang et al. (2007) by using the zenith tropospheric delay (ZTD) product consistently reprocessed throughout the period with the same approach (Wang et al. 2013). Such a consistent reprocessing improves the long-term stability of the GPS PW data and enhances its value for climate studies. The GPS PW monthly anomaly time series have been visually examined, and any sites with obvious discontinuities are not included in this analysis. Efforts to homogenize the GPS PW data are also under way (Ning et al. 2016b) and are beyond the scope of this study. The GPS PW data are attractive for climate trend analysis because of their long-term stability and more importantly, because their high temporal resolution enables us to study the unknown diurnal asymmetry of the PW trend.

Major artificial discontinuities in the long-term radiosonde records must be removed before they can be used for climate trend analysis. The radiosonde humidity data used in this study were homogenized using a statistical approach by Dai et al. (2011), combined with

the removal of the mean bias in the most widely used radiosonde, Vaisala RS92 (Wang et al. 2013). Two statistical tests were used to detect change points, which are most apparent in histograms and occurrence frequencies of the daily dewpoint depression (DPD): a variant of the Kolmogorov–Smirnov (K–S) test for changes in distributions and the penalized maximal  $F$  test (PMFred) for mean shifts in the occurrence frequency for different bins of DPD (Dai et al. 2011). Then the breakpoint adjustment was made using a quantile-matching algorithm. The PW from the radiosonde data was derived by integrating the water vapor content from the surface to 100 hPa. In calculating the PW trend for 1995–2011 using the GPS and radiosonde data, we required at least 10 days with data for monthly mean calculations, at least 2/3 of the months with valid data (136 months for 1995–2011), and at least 9 years with data for each month to calculate monthly mean climatology. There were 117 and 554 stations for the GPS and radiosonde data (Fig. 1), respectively, that met these requirements and were used in this study.

The MWR satellite PW data were obtained by combining monthly averaged oceanic retrievals of PW into a single dataset spanning the period from 1988 to 2015. The data used here were the version-7 retrievals produced by Remote Sensing Systems and include measurements made by SSM/I, SSMIS, AMSR-E, and WindSat (Remote Sensing Systems 2013). Measurements of PW made by coorbiting microwave radiometers are in very good agreement with each other. For overlap time series longer than 24 months, the ocean-only, global-mean vapor trends for individual satellites differ by less than  $0.05 \text{ mm decade}^{-1}$  from the multisatellite merged product. The ocean-only trend in the merged product also agrees to within  $0.05 \text{ mm decade}^{-1}$  with the trend obtained from the Tropical Rainfall Measuring Mission (TRMM) Microwave Imager (TMI) over the  $38^\circ\text{S}$ – $38^\circ\text{N}$  latitude band

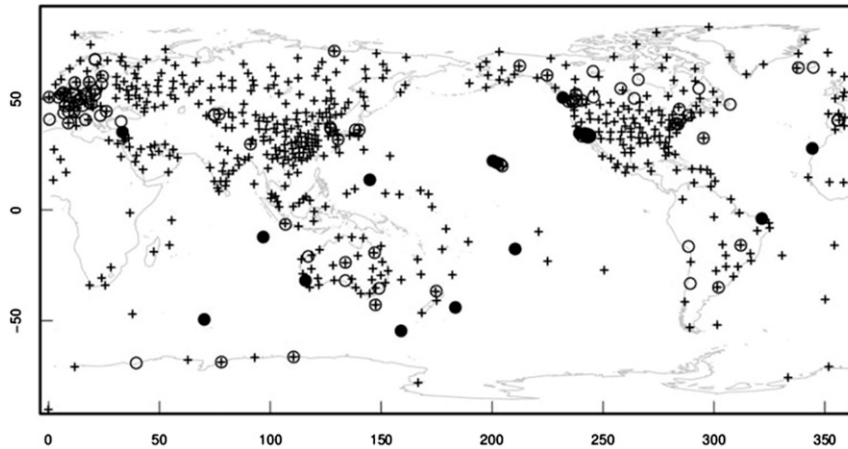


FIG. 1. The locations of the 117 GPS stations (circles), the 554 radiosonde stations (crosses), and the 15 stations (dots) where GPS, radiosonde, and MWR data are all available.

sampled by TMI (Wentz 2015). The TMI data are not directly used to construct the merged product and thus serve as a calibration reference. The consistency in PW trends among coorbiting radiometers gives us confidence in the combined MWR satellite PW data.

Two surface temperature datasets (Table 1) were used to study temperature trends and their correlations with the PW trends. They include the Global Historical Climatology Network–monthly (GHCN-M) version 3 dataset of monthly mean surface air temperatures, which was developed based on global land surface station data and was improved over its previous versions with new quality control and advanced techniques for removing data inhomogeneities (Menne and Williams 2009; Lawrimore et al. 2011). Besides mean surface temperature, GHCN-M also includes monthly means of daily maximum and minimum surface temperatures. The other temperature dataset used here is the NOAA/NCDC gridded monthly temperature anomaly dataset, which was created from the Extended Reconstructed Sea Surface Temperature (ERSST) version 3b (v3b) over oceans (Smith et al. 2008) and GHCN-M over land. The station GHCN-M data were matched with the radiosonde or GPS PW data by requiring the station separation of equal or less than 100 km horizontally and 500 m vertically and were used for calculations of the correlations between station PW and surface temperatures ( $T_{\text{sfc}}$ ,  $T_{\text{max}}$ , or  $T_{\text{min}}$ ). The NOAA/NCDC gridded data over land were used for global maps and averages of surface temperature (e.g., see Figs. 4b, 5b, 6, and 7). In addition, we also include monthly surface temperature and humidity data over oceans from the International Comprehensive Ocean–Atmosphere Dataset (ICOADS) release 2.5 on a  $1^\circ \times 1^\circ$  grid (Slutz et al. 1985; Woodruff et al. 2011), monthly mean surface humidity anomalies

from the gridded global land surface humidity dataset on a  $5^\circ \times 5^\circ$  grid (HadISDH) (Willett et al. 2014), and the hourly surface data at over 6000 global land stations from the global subdaily station dataset (HadISD) (Dunn et al. 2012) (Table 1). Despite improvements, the latest ICOADS only samples  $\sim 50\%$ – $60\%$  of the global oceans. Given the uneven distribution of  $>3000$  land stations over time and space used to create the gridded HadISDH data, sampling uncertainty exists and is estimated. (Since we used the ICOADS and HadISDH data only for Fig. 10, their spatial sampling issues likely have some impacts on the conclusions based on Fig. 10.)

Linear trends in this study were calculated using the Sen estimate of the slope (Sen 1968), which is more robust than the least squares fitting, especially for skewed data (Rousseeuw and Leroy 2003). We compared the PW linear trends derived from the least squares fitting with that from the Sen method and found (not shown) that they agree well with each other with a RMS difference of  $\sim 0.2 \text{ mm decade}^{-1}$ , but the Sen method is less sensitive to the beginning and ending values for stations with sparse data.

Collocated GPS and radiosonde stations and MWR grid boxes were used to compare PW trends from these independent measurements (Fig. 1). We required the collocated GPS and radiosonde stations to be within 50 km horizontally and 100 m vertically, and there were 31 such stations. There were 15 island or coast GPS stations that had collocated  $1^\circ \times 1^\circ$  grid boxes with MWR PW data available. Monthly mean PW anomalies were calculated for each dataset by removing its monthly climatology of 1997–2010 from the monthly data, and then the linear trend was calculated from the monthly anomaly series at each radiosonde and GPS station and MWR  $1^\circ \times 1^\circ$  ocean box.

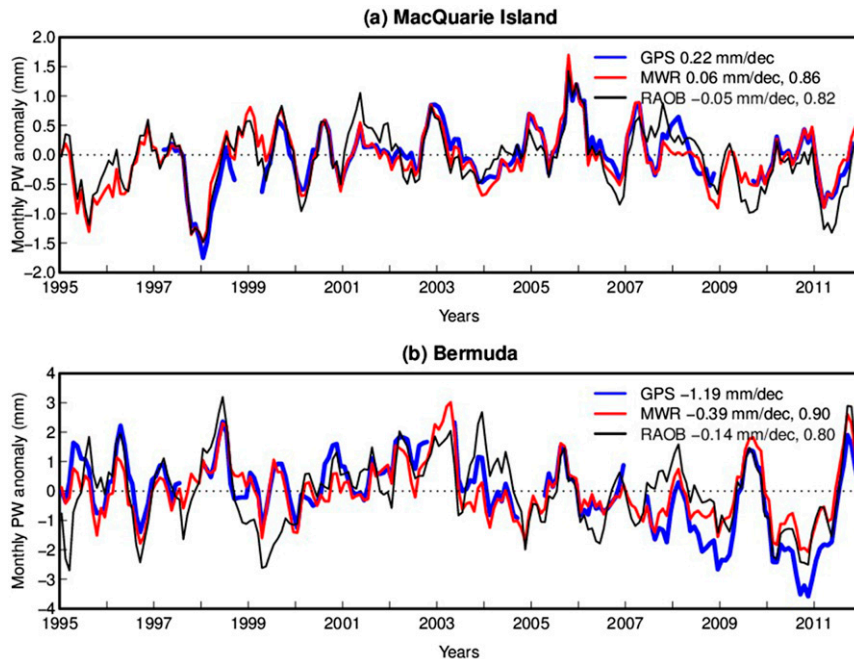


FIG. 2. Time series of monthly PW anomalies for 1995–2011 from the GPS (blue), MWR (red), and raob (black) observations at (a) MacQuarie Island ( $54.5^{\circ}\text{S}$ ,  $158.94^{\circ}\text{E}$ ) and (b) Bermuda ( $32.37^{\circ}\text{N}$ ,  $64.68^{\circ}\text{W}$ ). The PW linear trends ( $\text{mm decade}^{-1}$ ) and correlation coefficients between GPS and MWR or raob are given in the legends.

The PW trends from 1995–2011 and 1988–2011 at the 554 radiosonde stations were first computed and then gridded onto a  $0.5^{\circ} \times 0.5^{\circ}$  grid using a search radius of 1000 km using inverse distance-weighted averaging of all station data within the radius. Atmospheric temperature and humidity fields have a spatial correlation distance around 1000–1200 km, which is often used as the search radius in gridding their anomalies (Mitchell and Jones 2005). Then the values on all  $0.5^{\circ}$  grid boxes within each  $2.5^{\circ}$  box were averaged to derive PW anomalies on a  $2.5^{\circ} \times 2.5^{\circ}$  grid. The same gridding method was applied to the PW versus  $T_s$  correlation coefficients and the  $d\ln\text{PW}/dT_s$  ratio over land shown in section 4. Since the  $T_s$  data over oceans are on a  $5^{\circ} \times 5^{\circ}$  grid, the MWR data on a  $1^{\circ} \times 1^{\circ}$  box are first averaged onto a  $5^{\circ} \times 5^{\circ}$  grid box to calculate the correlation and ratio over oceans shown in section 4. Time series of global-mean monthly PW anomalies from the radiosonde and MWR data shown in Fig. 6 were computed from gridded anomaly data using gridbox area as weighting, while the mean PW time series for GPS were derived simply by averaging over all the 117 stations given their limited spatial coverage.

### 3. Global PW trend analysis

Figure 2 presents two examples from two island stations (MacQuarie Island and Bermuda), where PW data

are available from all three datasets. The three PW time series are highly correlated with a correlation coefficient  $r$  exceeding 0.8 at both stations, which is statistically significant above the 99% level (Fig. 2). This is also true for other collocated stations, with the  $r$  between GPS and MWR being higher than that between GPS and raob (Fig. 3a). For the MacQuarie Island and Bermuda stations, the PW trends for 1995–2011 derived from the GPS data have much larger magnitudes than that from the radiosonde and MWR (Fig. 2). For Bermuda, the larger negative PW trend from the GPS data might be due to the inhomogeneity in the GPS data (a drop in PW around February 2007), which is evident in comparisons with MWR and radiosonde data (see Fig. S2 in Mears et al. 2015).

The PW trends from 26 collocated radiosonde and GPS sites (21 sites for MWR vs GPS) are compared in Fig. 3. Five other collocated GPS-radiosonde stations are excluded in Fig. 3 because of sparse observations, unrealistically large trends in the radiosonde dataset, or large differences in radiosonde trends between 1995–2011 and 1973–2011. The PW trends from the collocated GPS and radiosonde or MWR sites are correlated, although the correlation of 0.36 between the GPS and radiosonde trends is insignificant (Fig. 3b). However, the trends are relatively weak in these short records (1995–2011) with large short-term variations, and most of them

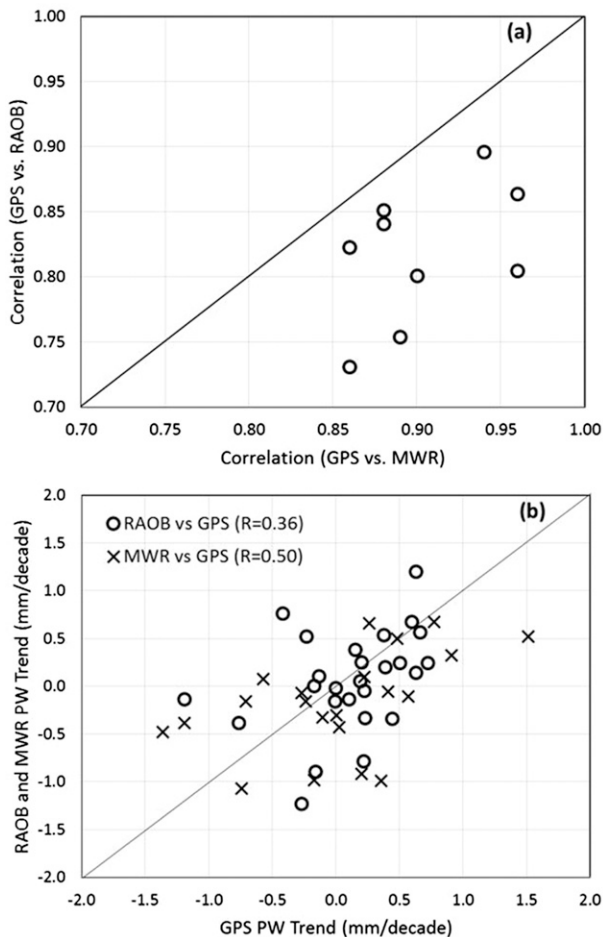


FIG. 3. (a) Comparisons of correlation coefficients between GPS and raob PW monthly anomaly time series from 1995 to 2011 and that between GPS and MWR at nine stations where all three datasets are available. (b) Comparisons of the 1995–2011 PW trends ( $\text{mm decade}^{-1}$ ), estimated from monthly anomalies) between the GPS and raob (circles) or MWR (crosses) data at 26 (for raob) or 21 (for MWR) collocated stations, respectively. The correlation coefficients are given in the legend.

are statistically insignificant (i.e., resulting from random noises that should reduce the correlation among the three datasets). Nevertheless, the spatial variations in the PW trends from 1995 to 2011 are generally consistent among the three datasets. Some of the scattering in Fig. 3b likely results from large uncertainties in trend estimates as a result of the short record length (17 years), large interseasonal and interannual PW variability, and potential inhomogeneity in the GPS PW data. In summary, the strong correlation between the GPS and radiosonde or MWR monthly PW anomaly time series and the broad agreement in their linear trends encourage us to use the three datasets together in space (but not in time) to study PW trends from 1995 to 2011 over the globe. Note that the three datasets were not merged in

time at any given location and not averaged at any given time and location.

The gridded PW trends from 1995 to 2011 from radiosonde data over land were merged with that over oceans derived from the MWR data to create a combined map of PW trends from 1995 to 2011 (Fig. 4a). This allows us, for the first time, to estimate PW trends over the whole globe (besides the polar regions) using observational data. The trends derived from the GPS data at 117 stations are also presented in Fig. 4a by the colored circles. The PW trends from the GPS data are generally in agreement with the radiosonde or MWR data (see discussions above). The homogenized radiosonde data show spatially coherent trends over land, such as positive trends over inland Australia but negative trends along its western coasts. In addition, consistent trends along coastal areas are seen between the radiosonde and MWR data. Some island and coastal radiosonde stations over the western Pacific region show large negative trends that are inconsistent with the surrounding regions. Visual examination of the radiosonde PW data indicated that the decreasing trends resulted from apparent PW drops sometime after 2008, which are most likely associated with radiosonde type changes. Note that the homogenization was only done for discontinuities at least 12 months before February 2009 by Dai et al. (2011). Therefore, these radiosonde stations with potential discontinuities after 2008 in the western Pacific were not included in our global land PW trend analysis (as shown in Fig. 6).

Figure 4a shows that PW trends over land are positive along the coast of the U.S. Northeast and Eurasia as well as the interior of Australia and Europe. The PW trends over the Pacific Ocean show a “sandwich” shape with positive trends in the narrow intertropical convergence zone (ITCZ) bounded by negative trends to the north and south. The negative trends expand to cover most of the eastern Pacific around the western coasts of the Americas. Even larger positive PW trends are seen over the central North and South Pacific and the western tropical Pacific (Fig. 4a). Using MWR PW data from 1988 to 2003, Trenberth et al. (2005) also showed positive PW trends over the Pacific ITCZ and the North and South Pacific but with fewer drying areas over the Pacific compared with Fig. 4a. They concluded that the 1988–2003 PW trend is explained largely by the change associated with the 1997/98 El Niño that appears to concur with a phase change of the interdecadal Pacific oscillation (IPO) from a warm period from 1977 to 1998 to a cold phase from 1999 to present (Dai 2013; Dong and Dai 2015). This suggests that PW trends for the recent periods that include the 1997/98 event will likely be similar, which is confirmed by our comparisons of trends

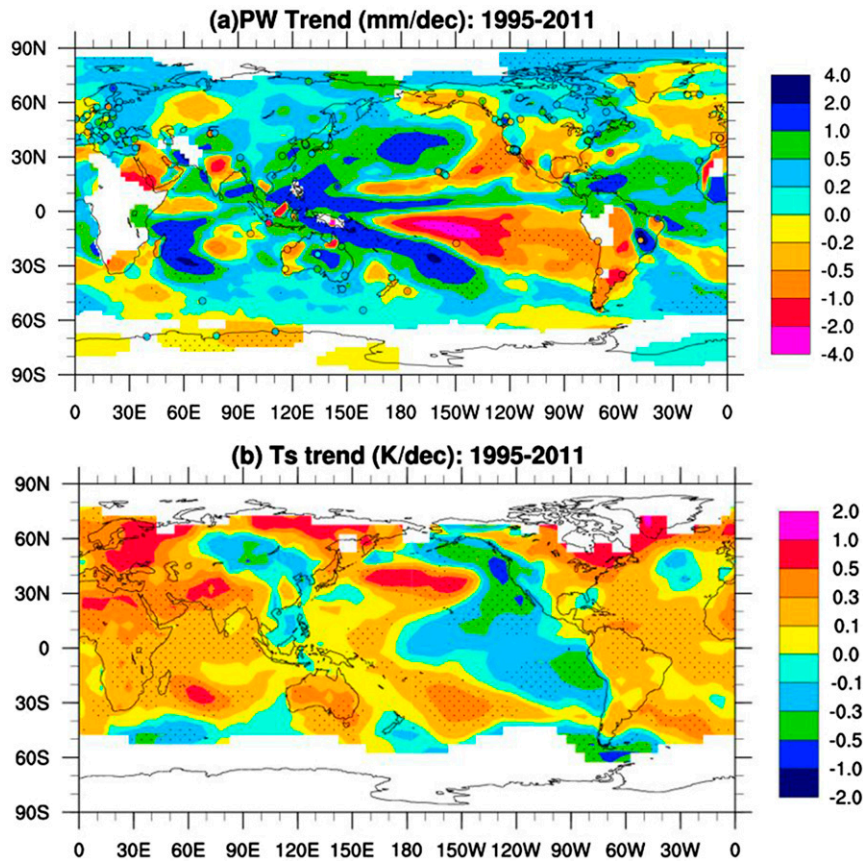


FIG. 4. (a) Global maps of PW trends from 1995 to 2011 estimated based on PW data from 117 GPS (circles) and 554 radiosonde stations over land and MWR data over oceans. (b) As in (a), but for  $T_s$  based on NCDC gridded  $T_s$  data. The stippled areas represent statistical significance at the 5% level.

for 1995–2011 and 1988–2011 (Fig. 5a). The Atlantic and Indian Oceans are dominated by moistening trends. The general patterns of the PW trends over oceans are consistent with those shown in IPCC AR4 (Trenberth et al. 2007) and AR5 (Hartmann et al. 2013) for the periods of 1988–2004 and 1988–2012, respectively, using the MWR data.

The PW trend map for 1988–2011 was also computed using the radiosonde and MWR data (Fig. 5a). Figure 5a shows smoother spatial patterns than the 1995–2011 trend map (Fig. 4a), but the two are largely similar. Compared with Fig. 4a, Fig. 5a has more uniform positive values over land and smaller magnitudes over the Pacific and Indian Ocean, as the trends estimated using the shorter records likely contain more noise. This suggests that the moistening trend over land is likely to be more robust in the longer records. This is further supported by the domination of positive trends for 1973–2011 in the radiosonde data (not shown). The spatial patterns of the PW trends over oceans are quite stable

for 1995–2011 and 1988–2011, but the amplitudes of the trends are more pronounced for the shorter period (Figs. 4a and 5a).

Time series of global-mean monthly PW anomalies were derived from the GPS, radiosonde, and MWR data (Fig. 6). It is evident that global-mean PW increases generally with time over both land and oceans during recent decades, at a rate of  $0.26 \pm 0.08$ ,  $0.24 \pm 0.03$ , and  $0.34 \pm 0.04$  mm decade<sup>-1</sup> based on the GPS (1995–2011), radiosonde (1973–2011), and MWR (1988–2011) data, respectively (Fig. 6). The trends are statistically significant at the 5% level for radiosonde and MWR but at the 10% level for GPS. Despite the limited spatial coverage of the GPS data (only 117 stations; cf. Fig. 1), they show interannual variations and long-term changes similar to those in the radiosonde data (Fig. 6a). The PW trends are smaller over land than over oceans and during 1995–2011 than 1988–2011 (Fig. 7).

We emphasize that the PW trend estimates for the recent decades are likely influenced by considerable

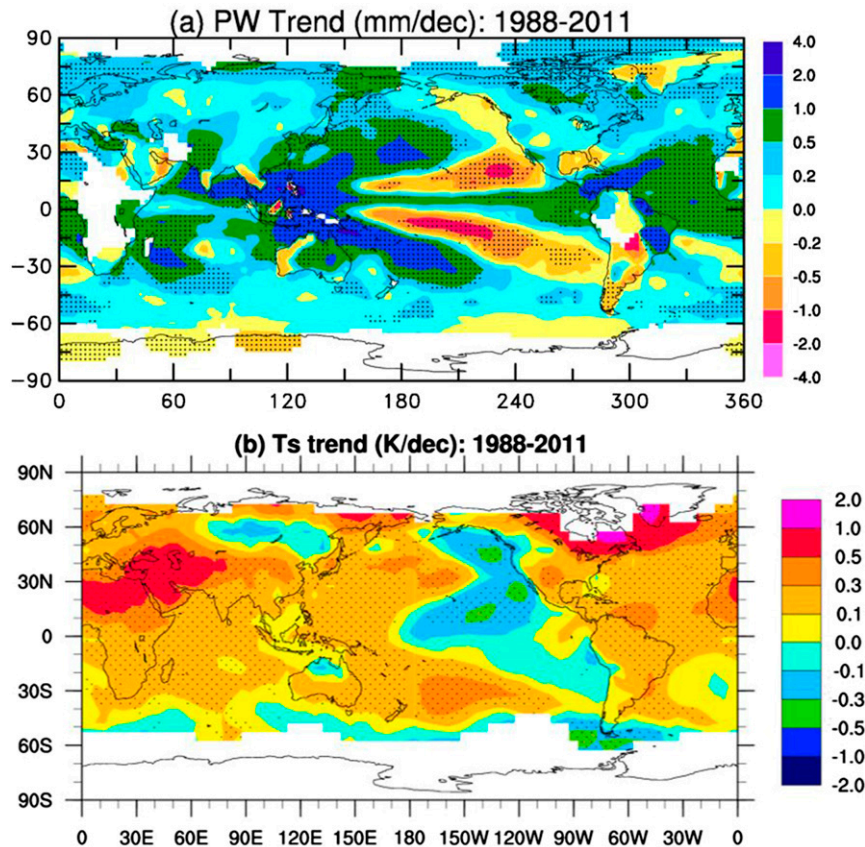


FIG. 5. As in Fig. 4, but for the period from 1988 to 2011 and using radiosonde and MWR PW data only. The stippled areas represent statistical significance at the 5% level.

sampling errors and large interannual variations (Fig. 6), which are usually linked to ENSO events, such as the maxima in 1987/88, 1997/98, and 2009/10 associated with El Niño events and the minima in 1988/89, 1992/93, 1999/2000, 2007/08, and late 2010/11 associated with La Niña events (Fig. 6). The PW and temperature decreases during 1992/93 are also likely caused by the cooling induced by the Pinatubo volcanic eruption in June 1991 (Trenberth and Dai 2007).

#### 4. PW–temperature relationship

The PW trends and interannual variations are correlated with temperatures, as shown previously (e.g., Zhao et al. 2012). Here we discuss the PW versus surface temperature  $T_s$  relationship briefly, based on Figs. 5, 6, and 8. Figure 5 shows that the areas with large positive PW trends generally have warming trends, such as the U.S. Northeast, Europe, Australia, the central North and South Pacific, and the southern Indian Ocean. Over the tropical central and eastern Pacific and a few other regions (e.g., central Asia), some cooling occurred

during 1988–2011 primarily because of the phase change of the IPO from the peak warm phase around 1993 to the near-lowest cold phase around 2012 (Fig. 5b; Dai 2013; Dai et al. 2015; Dong and Dai 2015). Associated with this cooling, PW also decreased or changed little over these regions, except the Pacific ITCZ where PW increased for reasons unknown. Despite this inconsistency, overall the PW and surface temperature trend patterns for 1988–2011 (Fig. 5) are positively correlated with a spatial correlation coefficient of 0.44, as one would expect from the fact that atmospheric relative humidity usually changes little (Dai 2006; Zhao et al. 2012), while saturation vapor pressure increases with air temperature. We analyzed surface humidity data and found that the trend patterns for surface specific humidity during 1988–2011 (not shown) are correlated with surface temperature trend patterns shown in Fig. 5b ( $r = 0.89$ ). Physically, PW should correlate more closely with lower-tropospheric temperature rather than surface temperature, as shown in Zhao et al. (2012) over China. Figure 7 shows that surface warming over land is more than twice that over ocean for both the 1995–2011

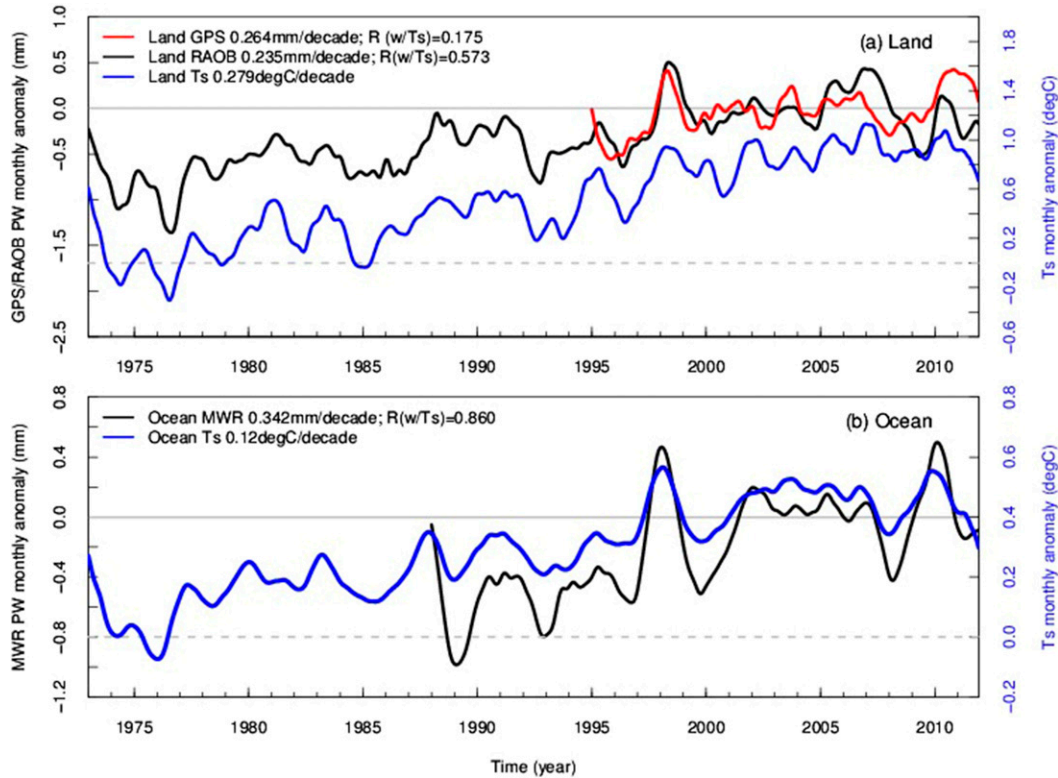


FIG. 6. Time series of global-mean monthly PW and  $T_s$  (blue line) anomalies over (a) land from the GPS (1995–2011) and raob (1973–2011) records, and (b) oceans from MWR (1988–2011). An 11-month running mean was applied to all the time series. Trends are calculated for the whole data period. Trends and correlation coefficients  $R$  between PW and  $T_s$  are given in the legends. Gray horizontal solid and dashed lines define zero values for the right and left y axes, respectively.

and 1988–2011 periods, while the PW trend is larger over ocean than over land. The correlation between PW and  $T_s$  monthly anomalies is positive and statistically significant over most regions except China, the U.S. Southwest, and the Amazon (Fig. 8). Zhao et al. (2012) showed that the PW and surface air temperature anomalies averaged over all of China for 1970–2008 are highly correlated. Such an inconsistency with Fig. 8 is mainly due to much weaker correlation between PW and  $T_s$  at individual stations than regional averages. We also found the same correlation coefficient of 0.76 as Zhao et al. (2012) for time series of 11-point moving-averaged PW and  $T_s$  anomalies averaged over China for 1973–2011. The correlation also becomes smaller for 1995–2011 and 2008–11 (0.5 and 0.45, respectively). As discussed later (see Fig. 10), the negative correlations between surface RH and  $T_s$  in China, the U.S. Southwest, and the Amazon can also partially explain the weaker correlations between PW and  $T_s$  shown in Fig. 8. Globally averaged land and ocean PW and  $T_s$  monthly anomalies are also significantly correlated, with stronger correlation over ocean than over land (Fig. 7).

As discussed in the introduction, the scaling ratio of the relative PW change with temperature  $d \ln PW / dT$  is often computed and used as a proxy for the increasing rate of atmospheric water vapor under global warming.

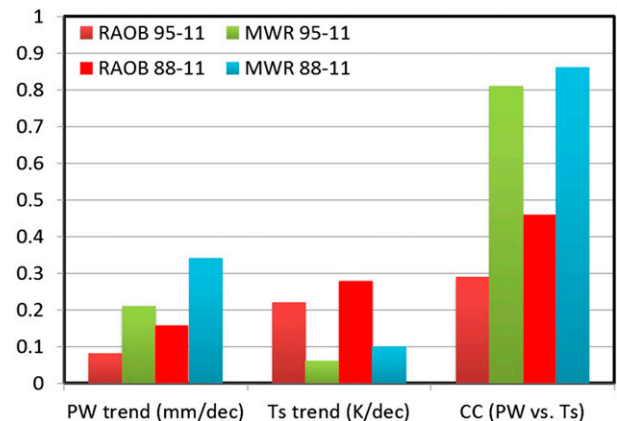


FIG. 7. Comparisons of PW trends,  $T_s$  trends, and correlation coefficients between PW and  $T_s$  using raob and MWR data for the 1995–2011 and 1988–2011 period. The colors for the  $T_s$  trend and CC (PW vs.  $T_s$ ) only refer to the time period shown in the legend.

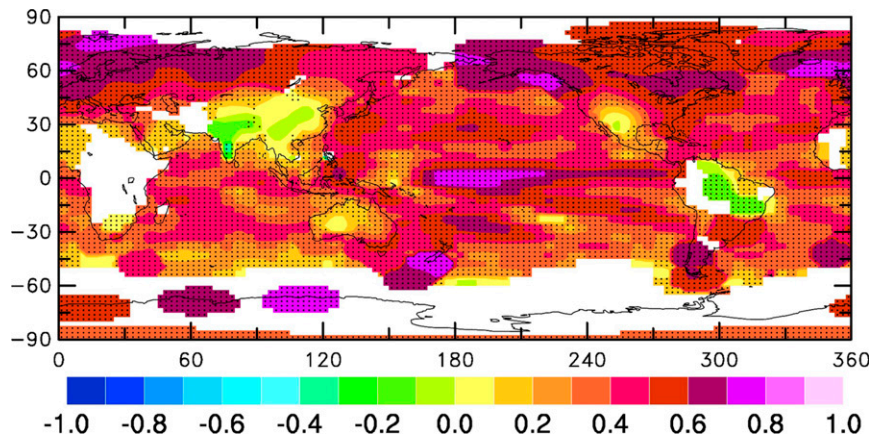


FIG. 8. Map of correlation coefficients between monthly PW and  $T_s$  anomalies from 1988 to 2011. The stippled areas represent statistically significant correlations at the 5% level.

If RH does not vary with temperature, then the scaling ratio should be around  $7\% \text{ K}^{-1}$  using typical globally averaged tropospheric temperatures. Previous studies have calculated this ratio using global and regional mean PW and temperature values and obtained a ratio around  $6\%–7\% \text{ K}^{-1}$  (e.g., Trenberth et al. 2005; Zhao et al. 2012). There are several questions associated with this simple scaling ratio: 1) Does RH vary with temperature? 2) On what temporal and spatial scales should the ratio be calculated? 3) Should surface temperature or lower-tropospheric mean temperature be used? And 4) how does the ratio vary spatially?

Here, we calculated this ratio using least squares linear fitting of the monthly relative PW and  $T_s$  anomalies during 1988–2011 at each  $5^\circ \times 5^\circ$  box over ocean and at each radiosonde station over land and then mapped the ratio onto a  $2.5^\circ \times 2.5^\circ$  grid (see section 2; Fig. 9). Thus, the scaling ratio shown in Fig. 9 is based primarily on the

interannual variations (but any long-term changes are also included). Figure 9 shows that the  $d \ln \text{PW} / dT_s$  ratio is generally larger over ocean than over land, and it tends to be above or around the expected value ( $\sim 7\% \text{ K}^{-1}$ ) from the C–C relation over oceans but well below  $7\% \text{ K}^{-1}$  over many land areas. The ratio ranges from  $4\%$  to  $6\% \text{ K}^{-1}$  over the North Pacific and Southern Ocean to  $10\%–14\% \text{ K}^{-1}$  over most tropical oceans. Over land, it is generally lowest over arid to semiarid areas, such as the Tibetan Plateau ( $\sim 2\% \text{ K}^{-1}$ ) and southwestern North America ( $2\%–3\% \text{ K}^{-1}$ ); however, the low values over northeastern South America may result partly from large sampling errors due to sparse data there. The land–ocean discrepancy and the spatial variability of this ratio are presumably associated with RH changes with temperature and the usage of  $T_s$  instead of the tropospheric air temperature  $T_a$ . Given that  $d \ln \text{PW} / dT_s \approx (d \ln q_s / dT_s) + (d \ln \text{RH} / dT_s)$ , where  $q_s$  is saturation

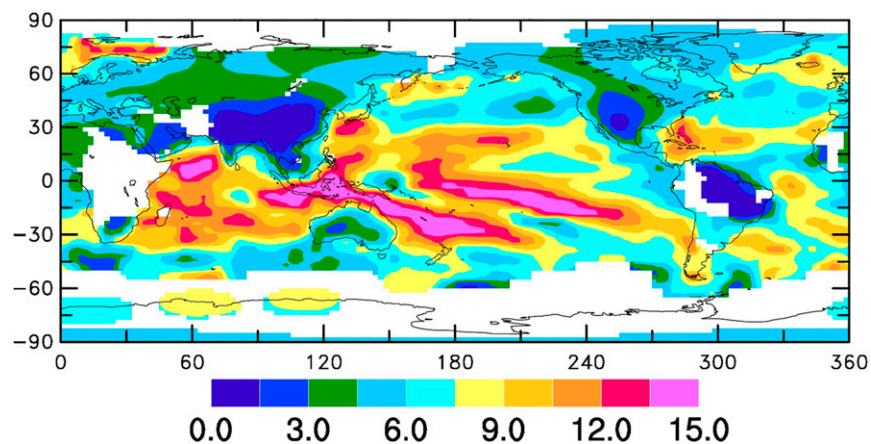


FIG. 9. Map of the scaling ratio of the percentage PW change with  $T_s$  ( $\% \text{ K}^{-1}$ ) using the linear least squares fitting of the anomaly data from 1988 to 2011.

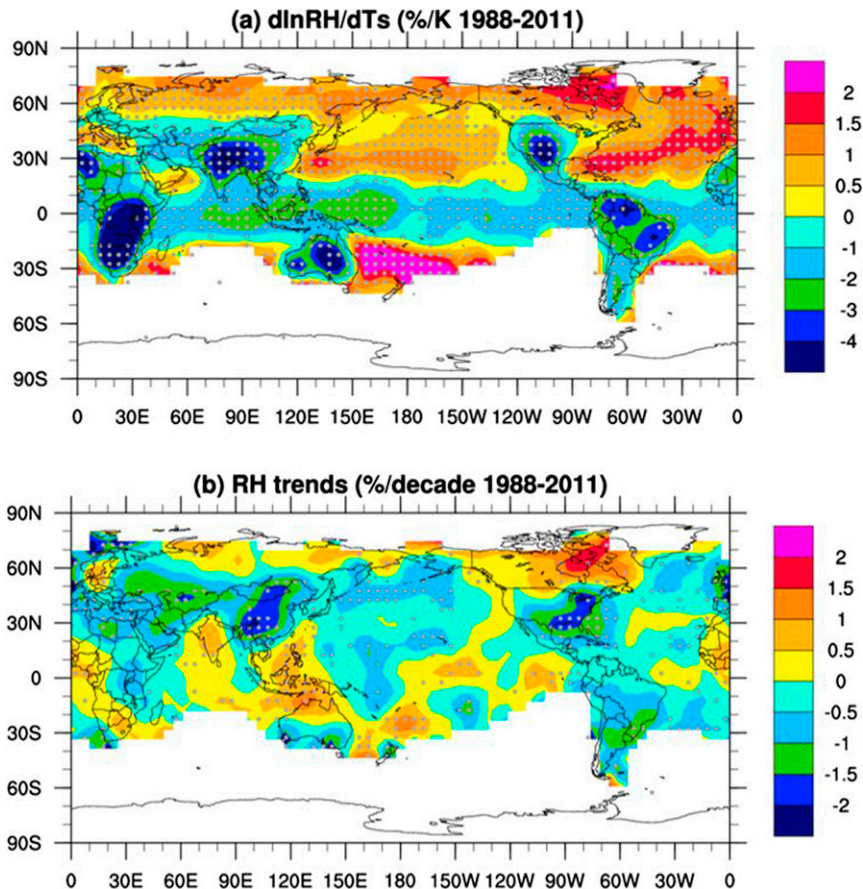


FIG. 10. (a) Map of the ratio of the percentage RH change with  $T_s$  ( $\% \text{ K}^{-1}$ ) using the linear least squares fitting of the anomaly data from 1988 to 2011. (b) Map of RH trends ( $\% \text{ decade}^{-1}$ ) from 1988 to 2011. The HadISDH dataset is used for land and the ICOADS dataset for oceans. The dotted boxes represent statistical significance at the 5% level.

specific humidity, and ignoring the difference between changes in  $T_s$  and  $T_a$ , for a  $d\ln PW/dT_s$  ratio above  $7\% \text{ K}^{-1}$ , RH has to increase with temperature, while RH should decrease with temperature where this ratio is below  $7\% \text{ K}^{-1}$ . To better understand the pattern of  $d\ln PW/dT_s$ , we calculated  $d\ln RH/dT_s$  using monthly anomalies of surface RH (which may not reflect lower-tropospheric RH) and  $T_s$  for 1988–2011 (Fig. 10a), as observational data for global tropospheric RH and  $T$  are not readily available. The land–ocean contrast and meridional variability of RH changes with  $T_s$  are generally consistent with what O’Gorman and Muller (2010) found from climate model simulations. Over oceans, RHs decrease with surface air temperature in the tropics but increase in the extratropics (Fig. 10a). The positive RH– $T_s$  relationship in the subtropical ocean contributes to the  $>7\% \text{ K}^{-1}$   $d\ln PW/dT_s$  ratio shown in Fig. 9. However, it is not clear why the signs and spatial patterns of  $d\ln RH/dT_s$  are not correlated with that of

$d\ln PW/dT_s$  in the tropical ocean, although sampling errors in the ICOADS data are large over tropical oceans. O’Gorman and Muller (2010) showed that the RH change rate with temperature at 500 hPa over tropical oceans is positive and larger than that at the surface. Therefore, the RH change with temperature in the lower troposphere and its contribution to  $d\ln PW/dT_s$  require further investigation. Over land, surface warming often leads to lower RH as surface evaporation cannot match atmospheric demand for moisture, which is confirmed by the negative RH– $T_s$  relationship in Fig. 10a. Therefore, the  $d\ln PW/dT_s$  ratio below  $7\% \text{ K}^{-1}$  over the majority of land can be explained by decreasing RHs with temperature.

The results from prior studies also shed light on what causes the observed  $d\ln PW/dT_s$  ratio shown in Fig. 9. Based on climate model simulations of the twenty-first-century climate, O’Gorman and Muller (2010) found that the  $d\ln PW/dT_s$  ratio has a strong dependence on

latitude and is larger in the tropics but smaller in the subtropics and midlatitudes than the C–C expected value. Deviations from the C–C value were attributed to decreases in RH with temperature at 500 hPa in the subtropics and midlatitudes and increases in the deep tropics (O’Gorman and Muller 2010). Wentz and Schabel (2000) concluded that the scaling of PW with  $T_s$  is larger than that with  $T_a$  over oceans mainly because the interannual change of  $T_a$  is larger than that of  $T_s$ . Also, greenhouse gas–induced long-term warming is larger in the troposphere than at the surface in the low latitudes (Myhre et al. 2013). Another feature displayed in Figs. 8 and 9 is that there is no significant correlation between PW and  $T_s$  and very low ( $2\%–3\% \text{ K}^{-1}$ )  $d\ln\text{PW}/dT_s$  ratios over southwestern North America whereas the northern and eastern United States show  $d\ln\text{PW}/dT_s$  values close to the C–C ratio. These results are consistent with the strong negative RH– $T$  correlation at the surface over the southwestern United States but negligible correlations at the same level in the eastern United States (Fig. 10a). Ross et al. (2002) showed similar spatial contrast in RH– $T$  correlations at 850 hPa and attributed such a spatial pattern to the sources of airflow. There are relatively warm and moist airflows from the south or cold and dry flow from the north in the eastern United States, but air flows over the arid western United States are from subsidence and are characterized by approximately constant specific humidity and negative RH– $T$  correlations (Ross et al. 2002). However, we think that surface soil moisture and evaporation may also be important in modulating the RH– $T$  and PW– $T$  relationships (Dai et al. 1999; Durre and Wallace 2001). Over the Tibetan Plateau and East Asia, both the PW– $T_s$  or RH– $T_s$  correlation and  $d\ln\text{PW}/dT_s$  or  $d\ln\text{RH}/dT_s$  ratio are low (Figs. 8 and 9). This may also be related to low evaporation over the dry Tibetan Plateau and downslope winds from the plateau to surrounding areas in the lower troposphere. Further investigations are needed on this unusual regional feature that appears to be robust.

## 5. Diurnal asymmetry

It is well known that surface diurnal temperature range (DTR) has decreased worldwide since the 1950s because of the larger warming in daily minimum temperatures  $T_{\min}$  than in daily maximum temperatures  $T_{\max}$  (e.g., Karl et al. 1993; Easterling et al. 1997; Vose et al. 2005). Given the strong connection between temperature and water vapor, one might expect a diurnal asymmetry in water vapor variations and trends. The high-resolution GPS PW data make it possible to study the diurnal asymmetry of the PW trends and PW– $T_s$

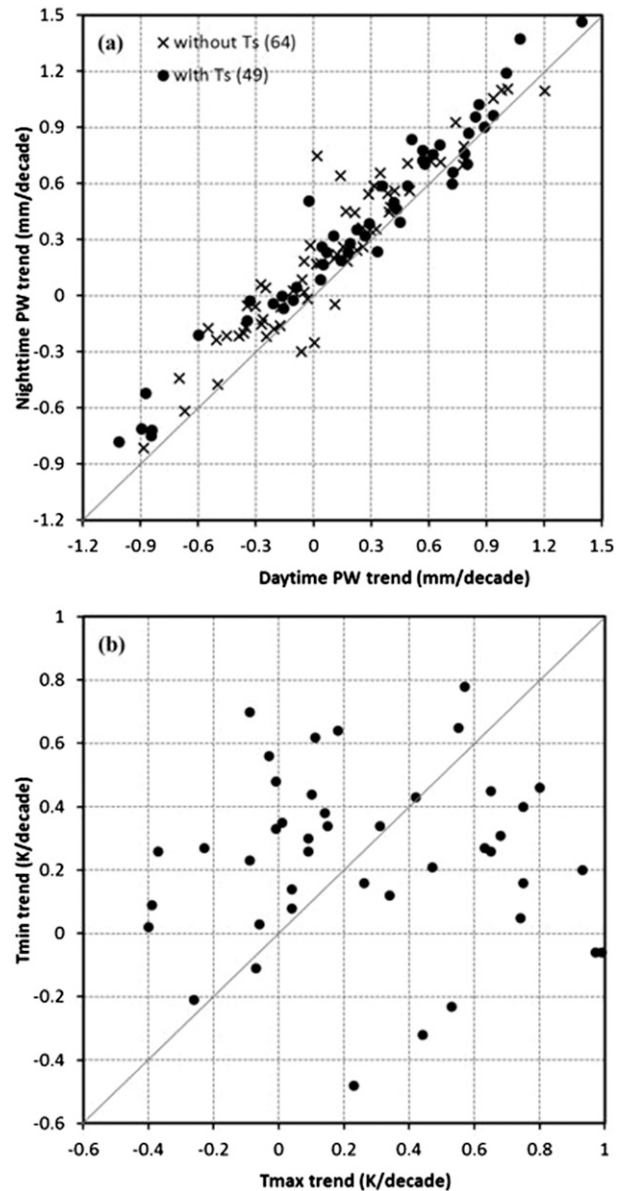


FIG. 11. (a) GPS PW trends ( $\text{mm decade}^{-1}$ ) from 1995 to 2011 for daytime ( $x$  axis) and nighttime ( $y$  axis). Solid circles and crosses are for sites with and without surface temperature data, respectively. (b)  $T_{\min}$  and  $T_{\max}$  trends ( $\text{K decade}^{-1}$ ) at 49 sites where surface temperature data are available.

scaling ratios. Figure 11a compares the daytime [0700–1900 local solar time (LST)] and nighttime (1900–0700 LST) PW trends for 1995–2011 at the 117 GPS stations. The PW trends are consistently larger at night than during the day at 91% of the stations.

We computed the PW trend for each observation time using the 2-hourly PW data at each GPS station and then fitted the diurnal variations in the PW trend using the diurnal (24 h) and semidiurnal (12 h) harmonics, following

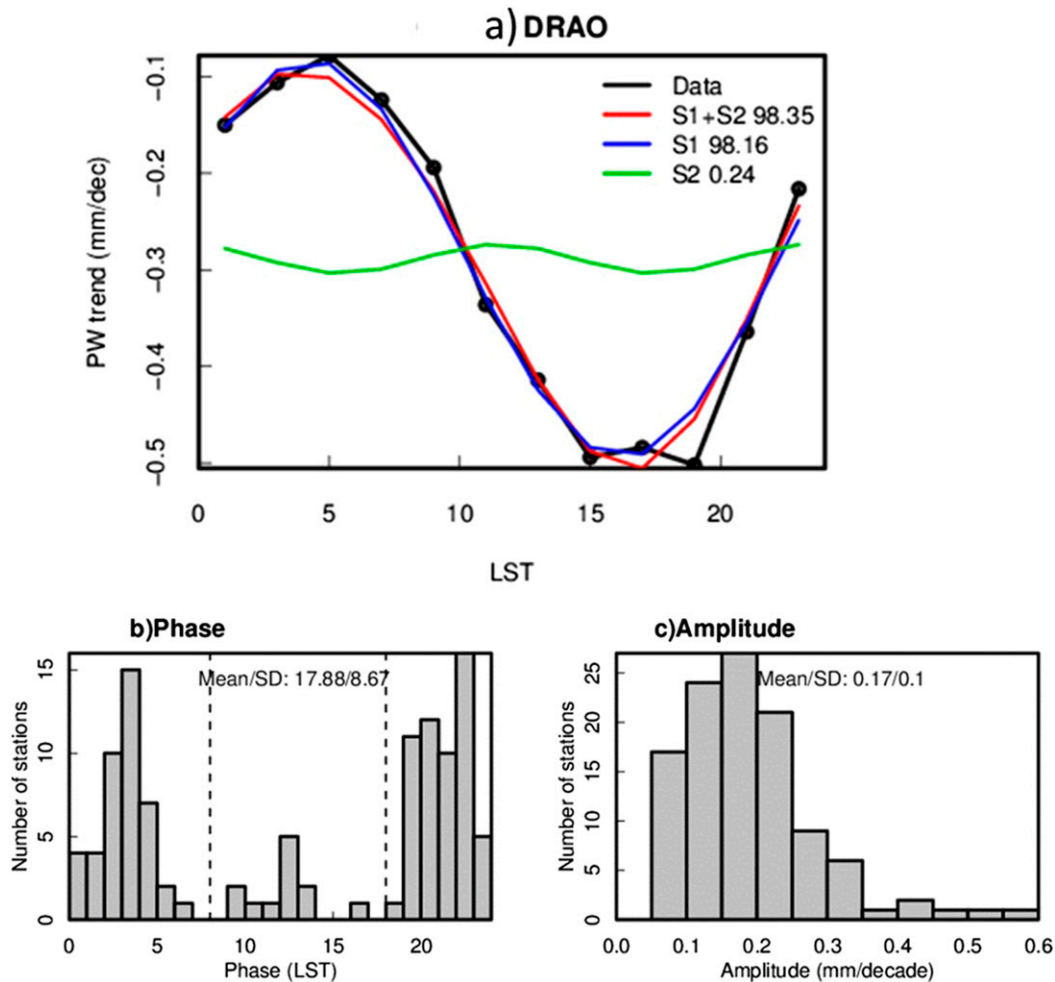


FIG. 12. (a) Diurnal variations of 2-hourly PW trends at the DRAO GPS site and the decomposed diurnal (S1) and semidiurnal (S2) components and the sum of two. The percentage of the variance explained by S1, S2, and S1 + S2 are also given in the legend. Histograms of (b) the phase (LST of the maximum in hours) and (c) amplitude of the diurnal harmonic of the PW trend for all 117 GPS stations. The mean and standard deviation among the stations are given in the legend.

Dai et al. (2002). At 66% of the stations, the diurnal cycle dominates the subdaily variability in the PW trends and explains 42% of the subdaily variance (only ~7% by the semidiurnal cycle) when averaged for all those stations. For example, at station DRAO (Penticton, Canada; 49.32°N, 119.62°W), the diurnal cycle explains 98.16% of the subdaily variability of the PW trend, while the contribution of the semidiurnal cycle is negligible (0.24%) (Fig. 12a). The PW trend peaks at night with a mean amplitude of 0.17 mm decade<sup>-1</sup> (Figs. 12b,c).

A detailed investigation of the causes of the PW trend diurnal asymmetry is beyond the scope of this study. Here we only provide a qualitative explanation and some hypotheses. The PW is the integration of specific

humidity  $q$ , which depends on both temperature and RH, and is controlled by  $q$  both near and above the surface [mainly the lower troposphere (LT)]. If the atmosphere is simplified into the surface layer and LT, four variables would affect the PW trend:  $T$  and RH near the surface and in the LT. It gets more complicated when we try to explain the diurnal asymmetry of the PW trend since the variable with the largest impacts on the PW trend may not be the one contributing most to the observed PW trend asymmetry. Here we study two variables, near-surface temperature and specific humidity.

Vose et al. (2005) found that global land averaged  $T_{\min}$  increased at a faster rate than  $T_{\max}$  from 1950 to 2004, but their warming trends are comparable from 1979 to 2004. Rohde et al. (2013) also found that the

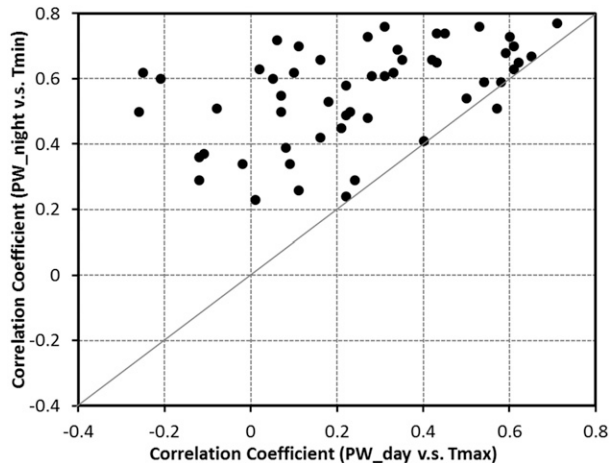


FIG. 13. Scatterplot of correlation coefficients between nighttime PW and  $T_{\min}$  and between daytime PW and  $T_{\max}$  monthly anomalies from 1995 to 2011 at the 49 stations with data. The gray diagonal line is the one-to-one line.

global land DTR decreased from 1900 to 1987, and thereafter it increased to 2011. We looked at the  $T_{\max}$  and  $T_{\min}$  trends during 1995–2011 at 49 GPS stations where nearby surface weather stations with  $T_{\min}$  and  $T_{\max}$  data were found within 100 km horizontally and 500 m vertically (Fig. 11b). The PW trends were found consistently larger during nighttime than daytime at these stations (Fig. 11a) but not for surface temperature (Fig. 11b). Thus, the recent DTR trend cannot explain the diurnal asymmetry in the PW trend.

We also examine the HadISD data at 30 stations where nearby GPS stations were found within 100 km horizontally and 500 m vertically. The comparisons of PW and surface specific humidity  $q$  trends between daytime and nighttime show that the trends are generally positive for PW but negative for surface  $q$ . It implies that the PW trend is likely related more to the temperature and humidity trends in a deeper lower-tropospheric layer and less impacted by the surface layer at these sites. Upper-air observations are needed to understand the  $q$  trends in the lower troposphere. An update of the homogenized radiosonde humidity data from Dai et al. (2011) is needed for this and other analyses. This is a major effort that is beyond the scope of this study.

The close association between PW and surface temperature has been presented and discussed in section 4. The remaining question is how such a relationship changes diurnally. Figure 13 shows the correlation coefficients between daytime PW and  $T_{\max}$  and between nighttime PW and  $T_{\min}$ . The correlation at night is positive, statistically significant, and systematically stronger than that during daytime. The daytime correlation

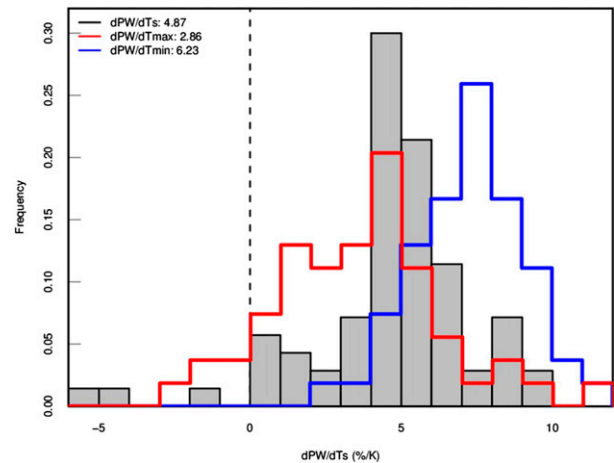


FIG. 14. Histograms of the scaling ratio  $d \ln PW/dT_s$  ( $\% K^{-1}$ ) at 49 GPS stations calculated from monthly anomalies from 1995 to 2011 of all-time PW and  $T_s$  (black, gray area), daytime PW and  $T_{\max}$  (red line), and nighttime PW and  $T_{\min}$  (blue line).

between PW and  $T_s$  is negative at some stations and often insignificant, implying that other factors such as clouds and surface evaporation are important [e.g., through their impacts on daytime  $T_s$ ; Dai et al. (1999)]. These results suggest that the relationship between PW and  $T_s$  at night is a better indicator of water vapor feedback (i.e., the coupling between  $T_s$  and water vapor content). Another interesting feature from Fig. 13 is that the day and night correlation coefficients are not strongly related at the stations; that is, a strong nighttime PW– $T_{\min}$  correlation is not usually associated with a strong daytime PW– $T_{\max}$  correlation at the same station. This again suggests that different mechanisms govern the PW– $T_s$  relationship during day and night. Such a diurnal asymmetry in the PW– $T_s$  correlation is also reflected in the scaling ratio  $d \ln PW/dT_s$  (Fig. 14). The ratio with  $T_{\min}$  is larger than that with  $T_{\max}$  and is closer to the C–C implied value ( $\sim 7\% K^{-1}$ ). The ratio with  $T_{\max}$  is smaller than the C–C implied value at most of the 49 stations and has a wider distribution, which suggests larger spatial variability and that the ratio is less constrained to the C–C relationship.

As mentioned above and studied previously (e.g., Dai et al. 1999), other factors such as clouds, aerosols, surface evaporation, and surface albedo can modulate maximum daytime  $T_s$  more than minimum nighttime  $T_s$ . This greatly weakens the coupling between water vapor and daytime  $T_s$  through longwave radiation because these other factors are often not correlated with atmospheric water vapor content. On the other hand, at night the shortwave effects disappear and surface evaporation is minimal (Dai et al. 1999), making the longwave greenhouse effect of water vapor a dominant factor (Zhang et al. 1995) that regulates nighttime  $T_s$ . This

qualitatively explains the stronger correlation between PW and  $T_s$  and the  $d\ln PW/dT_s$  ratio being closer to the  $7\% \text{ K}^{-1}$  at night than during the day. The additional factors influencing the daytime PW– $T_s$  relation also imply a wider distribution of  $d\ln PW/dT_s$  during the day.

## 6. Summary and discussion

To study water vapor changes over the globe, we have compared and used three global precipitable water (PW) datasets from homogenized radiosonde records, 2-hourly ground-based GPS measurements, and the newest version of satellite MWR observations. The combination of three PW datasets makes it possible to provide near-global estimates of the PW trend from 1988 (or 1995 for the GPS data) to 2011 over both land and ocean and to study the relationship between the PW and surface temperature  $T_s$  and the diurnal asymmetry in the PW trend and the PW– $T_s$  relationship. General agreements are found in the PW trend and its spatial variations among the three datasets at collocated stations. Main results are summarized below.

During the recent decades, PW has increased with time over both land and ocean regardless of the time period and dataset analyzed, with a global-mean trend of 0.26, 0.24, and  $0.34 \text{ mm decade}^{-1}$ , respectively, in the GPS (1995–2011), radiosonde (1973–2011), and MWR (1988–2011) records. The PW trends are smaller over land than over ocean, and they are smaller during 1995–2011 than 1988–2011, which is consistent with the slowdown in the global warming rate since around 2000 (Trenberth and Fasullo 2013; Dai et al. 2015). PW generally increased from 1988 to 2011 over Eurasia, inland Australia, many parts of North America, and most oceans except parts of the eastern and low-latitude Pacific where both PW and  $T_s$  decreased as a result of the IPO phase change around 1999 (Dai 2013; Dai et al. 2015; Dong and Dai 2015).

Global-mean PW monthly anomaly is well correlated with  $T_s$  on interannual to decadal time scales over both land and ocean, and the areas with positive PW trends generally show warming trends in  $T_s$ . The scaling ratio of the PW percentage changes with  $T_s$  ( $d\ln PW/dT_s$ ) shows large spatial variations, with generally larger values over ocean than over land. This ratio ranges from about  $4\%–7\% \text{ K}^{-1}$  over oceans poleward of  $30^\circ$  in both hemispheres to  $10\%–14\% \text{ K}^{-1}$  over most tropical oceans, but it is below the expected value ( $\sim 7\% \text{ K}^{-1}$ ) from the Clausius–Clapeyron relation over most land areas. The spatial variations in this scaling ratio are qualitatively consistent with model simulations (O’Gorman and Muller 2010) and are partially related to the differences in RH changes with surface temperatures over different regions.

The high temporal resolution of the GPS PW data made it possible to study the diurnal variations in the PW trends and the PW– $T_s$  relationship. It is found that the 1995–2011 PW trend at night is well correlated with that during the day, but it is consistently larger at night than during the day. The correlations between PW and  $T_s$  monthly anomalies during 1995–2011 also behave differently between day and night, with significant and positive PW– $T_s$  correlations at all stations at night but often insignificant and lower PW– $T_s$  correlations during the day. This day–night difference in the PW– $T_s$  relationship is attributed to additional impacts from clouds, aerosols, surface evaporation, and surface albedo on  $T_s$  (but not directly on PW except evaporation) during the day that should weaken the coupling between water vapor and  $T_s$ . The PW– $T_s$  scaling ratio  $d\ln PW/dT_s$  at night is also found to be larger and closer to the C–C implied value of  $7\% \text{ K}^{-1}$  than that during daytime.

Despite our efforts to combine different observations, large data gaps still exist over Africa and South America (Figs. 4 and 5). The cost-effectiveness, availability under all weather conditions, and unmanned operations of ground-based GPS PW measurements make it appealing to install more ground-based GPS receivers over those regions. International collaborations and support are required for such an effort. Diurnal variations in water vapor, its trends, and its relationship with temperature had remained largely unknown because of a lack of high temporal sampling in conventional radiosonde and satellite observations. This study took advantage of the high temporal resolution of the GPS PW data to study the diurnal asymmetry in PW trends and its correlation with  $T_s$ . However, continuous long-term records of GPS PW data are only available at  $\sim 117$  stations. Therefore, it is essential to reduce the data gaps in the GPS PW data and to maintain its quality, especially its temporal homogeneity as its record is getting longer.

Temporal homogeneity of climate records is most important for estimating long-term trends (Dai et al. 2011; Bodeker and Kremser 2015), while measurement uncertainties are important for estimating values for individual months or years. The well-characterized and traceable estimate of the measurement uncertainty is nontrivial. Global Climate Observing System (GCOS) Reference Upper-Air Network (GRUAN) is pioneering in providing such an estimate for certain radiosonde types (Immler et al. 2010; Dirksen et al. 2014; Bodeker et al. 2016). In this study, we have used homogenized radiosonde PW data records but had very limited information about the uncertainties in the PW data over the globe. The homogenization removes the major discontinuities resulting from changes in sampling or

instrumental biases over time. Thus, our use of homogenized PW data has largely removed the effect of time-varying measurement uncertainties on the estimated trends, as the remaining random measurement errors or constant biases should have very small effects on the estimated trends. Nevertheless, more efforts, such as GRUAN, are needed to estimate the uncertainties in the PW records from GPS, radiosondes, and MWR satellites. The radiosonde and GPS PW uncertainties to be included in the GRUAN data products (Dirksen et al. 2014; Ning et al. 2016a) will be helpful for PW homogenization and thus trend analyses. In addition, an updated and improved version of the homogenized radiosonde dataset of Dai et al. (2011) is also needed. Efforts to homogenize the GPS PW data are also under way (Ning et al. 2016b).

The positive water vapor feedback plays an important role in amplifying the anthropogenic greenhouse effect, but its amplitude still remains quite uncertain (Held and Soden 2000). Our findings of larger PW trends and better correlation between PW and surface temperature at night than during daytime suggest that the relationship of nighttime PW and  $T_s$  is a better indicator of the coupling between water vapor and  $T_s$ , and thus the nighttime data should be used to understand the water vapor feedback. Finally, although we have discussed the day–night differences in the PW trend and the PW– $T_s$  relationship and possible causes, more analyses are needed to fully understand the diurnal asymmetry found in this study.

**Acknowledgments.** This project is supported by NASA Grant NNX11AO25A through RSS's contract to UAlbany. Dai acknowledges the funding support from the U.S. National Science Foundation (Grant AGS-1353740), the U.S. Department of Energy's Office of Science (Award DE-SC0012602), and the U.S. National Oceanic and Atmospheric Administration (Award NA15OAR4310086). We thank Dr. Zaihua Ji from NCAR for providing the ICOADS data.

#### REFERENCES

- Bodeker, G., and S. Kremser, 2015: Techniques for analyses of trends in GRUAN data. *Atmos. Meas. Tech.*, **8**, 1673–1684, doi:10.5194/amt-8-1673-2015.
- , and Coauthors, 2016: Reference upper-air observations for climate: From concept to reality. *Bull. Amer. Meteor. Soc.*, **97**, 123–135, doi:10.1175/BAMS-D-14-00072.1.
- Dai, A., 2006: Recent climatology, variability, and trends in global surface humidity. *J. Climate*, **19**, 3589–3606, doi:10.1175/JCLI3816.1.
- , 2013: The influence of the inter-decadal Pacific oscillation on US precipitation during 1923–2010. *Climate Dyn.*, **41**, 633–646, doi:10.1007/s00382-012-1446-5.
- , K. E. Trenberth, and T. R. Karl, 1999: Effects of clouds, soil moisture, precipitation, and water vapor on diurnal temperature range. *J. Climate*, **12**, 2451–2473, doi:10.1175/1520-0442(1999)012<2451:EOCSMP>2.0.CO;2.
- , J. Wang, R. H. Ware, and T. Van Hove, 2002: Diurnal variation in water vapor over North America and its implications for sampling errors in radiosonde humidity. *J. Geophys. Res.*, **107**, 4090, doi:10.1029/2001JD000642.
- , —, P. W. Thorne, D. E. Parker, L. Haimberger, and X. L. Wang, 2011: A new approach to homogenize daily radiosonde humidity data. *J. Climate*, **24**, 965–991, doi:10.1175/2010JCLI3816.1.
- , H. Li, Y. Sun, L.-C. Hong, LinHo, C. Chou, and T. Zhou, 2013: The relative roles of upper and lower tropospheric thermal contrasts and tropical influences in driving Asian summer monsoons. *J. Geophys. Res. Atmos.*, **118**, 7024–7045, doi:10.1002/jgrd.50565.
- , J. C. Fyfe, S.-P. Xie, and X. Dai, 2015: Decadal modulation of global surface temperature by internal climate variability. *Nat. Climate Change*, **5**, 555–559, doi:10.1038/nclimate2605.
- Dirksen, R. J., M. Sommer, F. J. Immler, D. F. Hurst, R. Kivi, and H. Vömel, 2014: Reference quality upper-air measurements: GRUAN data processing for the Vaisala RS92 radiosonde. *Atmos. Meas. Tech.*, **7**, 4463–4490, doi:10.5194/amt-7-4463-2014.
- Dong, B., and A. Dai, 2015: The influence of the interdecadal Pacific oscillation on temperature and precipitation over the globe. *Climate Dyn.*, **45**, 2667–2681, doi:10.1007/s00382-015-2500-x.
- Dunn, R. J. H., K. M. Willett, P. W. Thorne, E. V. Woolley, I. Durre, A. Dai, D. E. Parker, and R. S. Vose, 2012: HadISD: A quality-controlled global synoptic report database for selected variables at long-term stations from 1973–2011. *Climate Past*, **8**, 1649–1679, doi:10.5194/cp-8-1649-2012.
- Durre, I., and J. M. Wallace, 2001: The warm season dip in diurnal temperature range over the eastern United States. *J. Climate*, **14**, 354–360, doi:10.1175/1520-0442(2001)014<0354:TWSDID>2.0.CO;2.
- Easterling, D. R., and Coauthors, 1997: Maximum and minimum temperature trends for the globe. *Science*, **277**, 364–367, doi:10.1126/science.277.5324.364.
- Flato, G., and Coauthors, 2013: Evaluation of climate models. *Climate Change 2013: The Physical Science Basis*, T. F. Stocker et al., Eds., Cambridge University Press, 741–866. [Available online at [http://www.climatechange2013.org/images/report/WG1AR5\\_Chapter09\\_FINAL.pdf](http://www.climatechange2013.org/images/report/WG1AR5_Chapter09_FINAL.pdf).]
- Gaffen, D. J., and R. J. Ross, 1999: Climatology and trends of U.S. surface humidity and temperature. *J. Climate*, **12**, 811–828, doi:10.1175/1520-0442(1999)012<0811:CATOUS>2.0.CO;2.
- Hartmann, D. L., and Coauthors, 2013: Observations: Atmosphere and surface. *Climate Change 2013: The Physical Science Basis*, T. F. Stocker et al., Eds., Cambridge University Press, 159–254. [Available online at [http://www.climatechange2013.org/images/report/WG1AR5\\_Chapter02\\_FINAL.pdf](http://www.climatechange2013.org/images/report/WG1AR5_Chapter02_FINAL.pdf).]
- Held, I. M., and B. J. Soden, 2000: Water vapor feedback and global warming. *Annu. Rev. Energy Environ.*, **25**, 441–475, doi:10.1146/annurev.energy.25.1.441.
- Immler, F. J., J. Dykema, T. Gardiner, D. N. Whiteman, P. W. Thorne, and H. Vömel, 2010: Reference quality upper-air measurements: Guidance for developing GRUAN data products. *Atmos. Meas. Tech.*, **3**, 1217–1231, doi:10.5194/amt-3-1217-2010.
- Isaac, V., and W. A. Van Wijngaarden, 2012: Surface water vapor pressure and temperature trends in North America during 1948–2010. *J. Climate*, **25**, 3599–3609, doi:10.1175/JCLI-D-11-00003.1.

- Karl, T. R., R. W. Knight, K. P. Gallo, and T. C. Peterson, 1993: A new perspective on recent global warming: Asymmetric trends of daily maximum and minimum temperature. *Bull. Amer. Meteor. Soc.*, **74**, 1007–1023, doi:10.1175/1520-0477(1993)074<1007:ANPORG>2.0.CO;2.
- Lawrimore, J. H., M. J. Menne, B. E. Gleason, C. N. Williams, D. B. Wuertz, R. S. Vose, and J. Rennie, 2011: An overview of the Global Historical Climatology Network monthly mean temperature data set, version 3. *J. Geophys. Res.*, **116**, D19121, doi:10.1029/2011JD016187.
- Mears, C. A., B. D. Santer, F. J. Wentz, K. E. Taylor, and M. F. Wehner, 2007: Relationship between temperature and precipitable water changes over tropical oceans. *Geophys. Res. Lett.*, **34**, L24709, doi:10.1029/2007GL031936.
- , J. Wang, D. Smith, and F. J. Wentz, 2015: Intercomparison of total precipitable water measurements made by satellite-borne microwave radiometers and ground-based GPS instruments. *J. Geophys. Res. Atmos.*, **120**, 2492–2504, doi:10.1002/2014JD022694.
- Menne, M. J., and C. N. Williams Jr., 2009: Homogenization of temperature series via pairwise comparisons. *J. Climate*, **22**, 1700–1717, doi:10.1175/2008JCLI2263.1.
- Mitchell, T. D., and P. D. Jones, 2005: An improved method of constructing a database of monthly climate observations and associated high-resolution grids. *Int. J. Climatol.*, **25**, 693–712, doi:10.1002/joc.1181.
- Myhre, G., and Coauthors, 2013: Anthropogenic and natural radiative forcing. *Climate Change 2013: The Physical Science Basis*, T. F. Stocker et al., Eds., Cambridge University Press, 659–740. [Available online at [https://www.ipcc.ch/pdf/assessment-report/ar5/wg1/WG1AR5\\_Chapter08\\_FINAL.pdf](https://www.ipcc.ch/pdf/assessment-report/ar5/wg1/WG1AR5_Chapter08_FINAL.pdf).]
- Ning, T., and Coauthors, 2016a: The uncertainty of the atmospheric integrated water vapour estimated from GNSS observations. *Atmos. Meas. Tech.*, **9**, 79–92, doi:10.5194/amt-9-79-2016.
- , J. Wickert, Z. Deng, S. Heise, G. Dick, S. Vey, and T. Schöne, 2016b: Homogenized time series of the atmospheric water vapor content obtained from the GNSS reprocessed data. *J. Climate*, **29**, 2443–2456, doi:10.1175/JCLI-D-15-0158.1.
- O’Gorman, P. A., and C. J. Muller, 2010: How closely do changes in surface and column water vapor follow Clausius–Clapeyron scaling in climate change simulations? *Environ. Res. Lett.*, **5**, 025207, doi:10.1088/1748-9326/5/2/025207.
- Remote Sensing Systems, 2013: Monthly mean total precipitable water data set on a 1 degree grid made from Remote Sensing Systems Version-7 Microwave Radiometer Data. Remote Sensing Systems. [Available online at [ftp://ftp.discover-earth.org/vapor/monthly\\_1deg/](ftp://ftp.discover-earth.org/vapor/monthly_1deg/).]
- Rohde, R., and Coauthors, 2013: A new estimate of the average Earth surface land temperature spanning 1753 to 2011. *Geoinf. Geostat.*, **1**, doi:10.4172/2327-4581.1000101.
- Ross, R. J., W. P. Elliott, and D. J. Seidel, 2002: Lower-tropospheric humidity–temperature relationships in radiosonde observations and atmospheric general circulation models. *J. Hydrometeorol.*, **3**, 26–38, doi:10.1175/1525-7541(2002)003<0026:LTHTRI>2.0.CO;2.
- Rousseeuw, P. J., and A. M. Leroy, 2003: *Robust Regression and Outlier Detection*. Wiley Series in Probability and Mathematical Statistics, Vol. 516, Wiley, 360 pp.
- Sen, P. K., 1968: Estimates of the regression coefficient based on Kendall’s tau. *J. Amer. Stat. Assoc.*, **63**, 1379–1389, doi:10.1080/01621459.1968.10480934.
- Shiu, C. J., S. C. Liu, and J. P. Chen, 2009: Diurnally asymmetric trends of temperature, humidity, and precipitation in Taiwan. *J. Climate*, **22**, 5635–5649, doi:10.1175/2009JCLI2514.1.
- Slutz, R. J., S. J. Lubker, J. D. Hiscox, S. D. Woodruff, R. L. Jenne, D. H. Joseph, P. M. Steurer, and J. D. Elms, 1985: Comprehensive ocean-atmosphere data set, release 1. NOAA Environmental Research Laboratories Rep., 268 pp.
- Smith, T. M., R. W. Reynolds, T. C. Peterson, and J. Lawrimore, 2008: Improvements to NOAA’s historical merged land–ocean surface temperature analysis (1880–2006). *J. Climate*, **21**, 2283–2296, doi:10.1175/2007JCLI2100.1.
- Trenberth, K. E., and A. Dai, 2007: Effects of Mount Pinatubo volcanic eruption on the hydrological cycle as an analog of geoengineering. *Geophys. Res. Lett.*, **34**, L15702, doi:10.1029/2007GL030524.
- , and J. Fasullo, 2013: An apparent hiatus in global warming? *Earth’s Future*, **1**, 19–32, doi:10.1002/2013EF000165.
- , A. Dai, R. M. Rasmussen, and D. B. Parsons, 2003: The changing character of precipitation. *Bull. Amer. Meteor. Soc.*, **84**, 1205–1217, doi:10.1175/BAMS-84-9-1205.
- , J. Fasullo, and L. Smith, 2005: Trends and variability in column-integrated atmospheric water vapor. *Climate Dyn.*, **24**, 741–758, doi:10.1007/s00382-005-0017-4.
- , and Coauthors, 2007: Observations: Surface and atmospheric climate change. *Climate Change 2007: The Physical Science Basis*, S. Solomon et al., Eds., Cambridge University Press, 235–336. [Available online at <https://www.ipcc.ch/pdf/assessment-report/ar4/wg1/ar4-wg1-chapter3.pdf>.]
- , J. T. Fasullo, and J. Kiehl, 2009: Earth’s global energy budget. *Bull. Amer. Meteor. Soc.*, **90**, 311–324, doi:10.1175/2008BAMS2634.1.
- Vose, R. S., D. R. Easterling, and B. Gleason, 2005: Maximum and minimum temperature trends for the globe: An update through 2004. *Geophys. Res. Lett.*, **32**, L23822, doi:10.1029/2005GL024379.
- Wagner, T., S. Beirle, M. Grzegorski, and U. Platt, 2006: Global trends (1996–2003) of total column precipitable water observed by Global Ozone Monitoring Experiment (GOME) on ERS-2 and their relation to near-surface temperature. *J. Geophys. Res.*, **111**, D12102, doi:10.1029/2005JD006523.
- Wang, J., L. Zhang, A. Dai, T. Van Hove, and J. Van Baelen, 2007: A near-global, 2-hourly data set of atmospheric precipitable water from ground-based GPS measurements. *J. Geophys. Res.*, **112**, D11107, doi:10.1029/2006JD007529.
- , —, —, F. Immler, M. Sommer, and H. Vömel, 2013: Radiation dry bias correction of Vaisala RS92 humidity data and its impacts on historical radiosonde data. *J. Atmos. Oceanic Technol.*, **30**, 197–214, doi:10.1175/JTECH-D-12-00113.1.
- Wang, J. X., and D. J. Gaffen, 2001: Late-twentieth-century climatology and trends of surface humidity and temperature in China. *J. Climate*, **14**, 2833–2845, doi:10.1175/1520-0442(2001)014<2833:LTCCAT>2.0.CO;2.
- Wentz, F. J., 1997: A well calibrated ocean algorithm for Special Sensor Microwave Imager. *J. Geophys. Res.*, **102**, 8703–8718, doi:10.1029/96JC01751.
- , 2015: A 17-year climate record of environmental parameters derived from the Tropical Rainfall Measuring Mission (TRMM) Microwave Imager. *J. Climate*, **28**, 6882–6902, doi:10.1175/JCLI-D-15-0155.1.
- , and M. Schabel, 2000: Precise climate monitoring using complementary satellite data sets. *Nature*, **403**, 414–416, doi:10.1038/35000184.

- , L. Ricciardulli, K. Hilburn, and C. Mears, 2007: How much more rain will global warming bring? *Science*, **317**, 233–235, doi:[10.1126/science.1140746](https://doi.org/10.1126/science.1140746).
- Willett, K. M., R. J. H. Dunn, P. W. Thorne, S. Bell, M. de Podesta, D. E. Parker, P. D. Jones, and C. N. Williams Jr., 2014: HadISDH land surface multi-variable humidity and temperature record for climate monitoring. *Climate Past*, **10**, 1983–2006, doi:[10.5194/cp-10-1983-2014](https://doi.org/10.5194/cp-10-1983-2014).
- Woodruff, S. D., and Coauthors, 2011: ICOADS release 2.5: Extensions and enhancements to the surface marine meteorological archive. *Int. J. Climatol.*, **31**, 951–967, doi:[10.1002/joc.2103](https://doi.org/10.1002/joc.2103).
- Zhang, Y.-C., W. B. Rossow, and A. A. Lacis, 1995: Calculation of surface and top of atmosphere radiative fluxes from physical quantities based on ISCCP data sets. Part 1: Methods and sensitivity to input data uncertainties. *J. Geophys. Res.*, **100**, 1149–1165, doi:[10.1029/94JD02747](https://doi.org/10.1029/94JD02747).
- Zhao, T., A. Dai, and J. Wang, 2012: Trends in tropospheric humidity from 1970 to 2008 over China from a homogenized radiosonde dataset. *J. Climate*, **25**, 4549–4567, doi:[10.1175/JCLI-D-11-00557.1](https://doi.org/10.1175/JCLI-D-11-00557.1).